Experiments in Fluids (2024) 65:181
https://doi.org/10.1007/s00348-024-03928-4

RESEARCH ARTICLE

Internal wave field generated by oscillating rough topography

Natasha Wilson[1] · **Julie Crockett**[1]

Received: 26 August 2024 / Revised: 11 November 2024 / Accepted: 13 November 2024

Abstract

Internal waves generated by oscillating topography with a series of ridges in a stratified medium are experimentally explored. Experiments represent oscillating tidal flow in the ocean where small-scale roughness on topography cannot be fully resolved in global circulation models, but the generated internal wave field can impact global mixing and ocean dynamics. Here, the influence of topography roughness is evaluated by including different numbers of ridges, with slopes equivalent to the edge slope of the full topography, on top of the original topography. Specifically, the internal wave field generated by a wide plateau shape is compared with the same shape except with three to six Gaussian ridges overlain on the plateau. In all scenarios, a complex pattern of internal waves generated by each ridge is observed. However, the results show as the number or width of ridges increases, the waves generated by the ridges near the center of the plateau decay very quickly and in the far field the internal wave field is indistinguishable from that generated by a smooth plateau. A non-dimensional number is suggested that accounts for both the number of ridges and overall topography width while defining a limit for which plateau-like internal wave generation is expected and this form of surface roughness may be neglected.

1 Introduction

Stably stratified fluids, such as the oceans, allow the generation and propagation of internal waves (Garett and Kunze 2007). When internal waves break, they transfer energy to the local water column through mixing. Of the 2 terawatts (TW) of energy available for mixing the ocean (Munk and Wunsch 1989), 1 TW originates from winds at the ocean surface (Wunsch 1998) and the other from the tides which are consistently generating internal waves as they force ocean water up and over (or around) bathymetry (Egbert and Ray 2000). Since internal waves can travel across ocean basins before breaking and mixing the local fluid, they alter on a global scale where the energy from the tides is finally dissipated and thus their quantification is essential to understanding global ocean processes (Scott et al. 2011; Nelson et al. 2020).

Significant research exploring flow over a single, symmetric, two-dimensional ridge such as Gaussian, sinusoid, Witch of Agnesi, or knife edge has shown that for low Excursion number, $Ex = p/w << 1$ (where p is the excursion length and w is the topography width at 1% amplitude in the direction of the flow), the range of wavenumbers in the generated internal wave field correlates with the range of wavelengths required to create the topography shape (Nappo 2002). However, when the scenario becomes supercritical, $\epsilon > 1$ (where ϵ is the ratio of the slope of the topography to the slope of the propagating internal wave beam), wave overturning and breaking may occur near the topography (Lamb 2014). Linear theory allows for analytical solutions for simple topographic shapes, while more complex topographies require a Green's function (Echeverri and Peacock 2010) or Fourier-series approach (Balmforth et al. 2002). As topography increases in complexity, the boundary layer, wave–wave interactions, overturning, and viscous damping become important.

Internal waves generated by two topographies in the vicinity of one another can result in complex interactions both during generation and propagation. The generated internal wave field is highly dependent on the relative size, including local slope, width, and amplitude, as well as position of each individual topography (Echeverri and Peacock 2010; Echeverri et al. 2011). Specifically, Echeverri and

---

Natasha Wilson and Julie Crockett have contributed equally to this work.

✉ Julie Crockett
crockettj@byu.edu

Natasha Wilson
natashawilson.pur@gmail.com

[1] Mechanical Engineering, Brigham Young University, 350 EB, Provo, UT 84602, USA

Peacock simulated variably spaced two-ridge configurations using a Green's function approach in uniform stratification and oscillating flow (Echeverri and Peacock 2010). In the case of two separated, repeated, and symmetric subcritical Gaussian ridges, Echeverri and Peacock found the internal waves generated by one ridge interfered with the waves generated by the other ridge causing wave scattering by the other ridge (Echeverri and Peacock 2010). More interactions between waves and a more complex wave field were observed when the two Gaussian ridges were mismatched (had different standard deviations).

When multiple topographies are present, a significant decrease in amplitude of the generated wave field has been observed in experiments and numerical models (Sutherland and Aguilar 2006; Zhang and Swinney 2014; Zhang et al. 2017), and when this reduced wave amplitude is used in global models, they better predict observations (Trossman et al. 2013; Klymak et al. 2021). Sutherland and Aguilar experimentally generated internal waves over and in the lee of spaced, repeated sinusoidal hills, triangles, and rectangles by towing the topography at a constant speed in uniform stratification (Sutherland and Aguilar 2006). They found that, contrary to linear theory, the internal wave amplitude directly over the topography was much smaller than the ridge heights due to trapped water between the shapes from boundary layer separation reducing the effective amplitude of the ridges. The trapped fluid between ridges also altered the effective shape of the topographies. Further similar experiments found that internal waves are excited by both lee waves and turbulence following the towed topography (Aguilar and Sutherland 2006).

Balmforth, Ierley, and Young calculated inviscid internal waves generated by separated repeating subcritical shapes including sinusoid, Gaussian, and several random topographies designed to have similar features to ocean floors (Balmforth et al. 2002). They found that internal waves were generated at the points of maximum slope on the topography and that in some cases topographies with criticality greater than 0.8 result in overturned buoyancy gradients and can therefore be statically unstable. For the random topography profiles, the generated internal wave field was found to be greatly dependent on the topography profile with energy conversion rates varying by a factor of two. They also found that increasing criticality does little to increase the conversion rate, but rather creates small-scale features in the internal waves. Other work involving multiple supercritical slope topographies demonstrates that the impact of local topography spacing and wave–wave interactions can be more significant than in the subcritical case, although the general result is still a suppression of radiated power in the generated internal wave field (Nycander 2006; Balmforth and Peacock 2009).

Much past work has been performed in experiments, simulations, and theory focusing on single-ridge topographies or spaced multi-ridge topographies. More work is needed to understand the generation and interaction of internal waves from an individual topography with multiple ridges. It is hypothesized that as more ridges are added for the same topography length, the internal wave field will deviate more from that created by a single-ridge topography and will instead approach the internal wave field generated by a smooth plateau topography of the same length. To this end, experiments are performed with oscillating multiple-ridge topographies. Three different plateau widths are defined and 3-6 internal ridges are superimposed on the plateau to model varying ridge roughness. Each width has a defined Gaussian slope for the ridges and the plateau edge.

2 Methods

2.1 Experimental setup

A clear acrylic tank (1 m, 2.5 m, 0.1 m) with stratified salt water was used in combination with the synthetic schlieren method developed by Sutherland and Dalziel to visualize the internal waves generated by oscillating the topographies (Sutherland et al. 1999; Dalziel et al. 2000). The narrow tank constrains the generated internal waves to two dimensions. The stratification profile was achieved by pumping a calculated volume of fresh and saltwater separately into a mixer and then the tank. Filtering material was layered along the sides and bottom of the tank to dampen internal wave reflections.

An analog Aichose specific gravity refractometer was used to determine the salinity of 1–2 mL of water sampled every 5 cm. For the top 10 cm of the water, the sampling spacing was reduced to 2 cm. A linear fit of the density data was used to obtain the slope of the density profile and thereby calculate the buoyancy frequency, N, defined by $N^2 = (-g/\rho_0)(\partial\rho/\partial z)$, where g is the acceleration due to gravity (9.81 m/s^2), ρ_0 is a reference density, $\partial\rho/\partial z$ is the vertical density change, and z is positive upwards. For the experiments accomplished here, N varied from 1.1–1.2 s^{-1}.

Each individual test had a slightly different oscillation frequency (ω) since waves with $\omega/N = 0.8$ were desired and each tank fill had a slightly different N value. Due to variability in the oscillating mechanism, values of ω/N ranged from 0.79 to 0.83. There were 15 minutes between tests to allow the water to settle, and the density profile was remeasured daily. If at any time (including the initial fill) the N value or linear profile were poor, or if a mixed region was observed near the topography, the tank was drained and refilled. Generally, the tank was refilled every 3 to 4 days.

2.2 Post processing

Images were captured using a jAi Cv-M4+Cl progressive scan camera positioned 2.5 m in front of the tank focused on a matrix of randomized black dots backlit behind the tank. The camera could image nominally a 0.5 x 0.6 m region, but since the topographies are all symmetric, only the waves generated on the right side were imaged in order to capture the largest possible region of a singular wave beam. The impact of temperature variations between the camera and tank was negligible in the synthetic Schlieren processing. Video frames were post-processed using DigiFlow (Dalziel Research Partners 2018) at 6 fps to obtain ΔN^2 in space and time. A Hilbert transform is applied to ΔN^2 to calculate $\Delta \widetilde{N}^2$ in wavenumber space. Frequencies below 0.3 s^{-1} and above 1.2 s^{-1} were removed to focus on the generated internal waves. Following the method of Wunsch and Brandt (2012) for a linear density gradient, the kinetic energy in the internal wave beam is calculated in wavenumber space using

$$KE = \frac{\omega^2 N^2}{k^2(N^2 - \omega^2)} \left| \frac{\Delta \widetilde{N}^2}{N^2} \right|^2 \tag{1}$$

where k is the horizontal wavenumber.

2.3 Topographies

To characterize the impact multiple ridges have on the generated internal wave field, eight topography styles are created, and to observe the impact of slope steepness, three different widths are applied to each of these eight styles resulting in 24 separate topography shape scenarios. All are defined by one or more Gaussian profiles having the same amplitude ($a = 4$ cm) and standard deviation.

$$h(x) = ae^{\left(\frac{-(x-b)^2}{2c^2}\right)} \tag{2}$$

where b shifts the ridge location horizontally and c determines the width. Three series of symmetric topographies are created: narrow, medium, and wide, where c values defining these topography widths are shown in Table 1. All topographies are 3D printed using fused deposition modeling and are uniform in depth to fill tank width and represent two-dimensional dynamics.

Also included in Table 1 are the expected wavenumbers based on the total topography width, k_t, and the expected wavenumber based on an estimate of the expected wavelength from the shape of the generating Gaussian, $k = 2\pi/\lambda_x$ where $\lambda_x = w + p$ (Lee and Crockett 2019). Here w is the Gaussian width at 1% height, p is the excursion length, and the subscripts n, m, and w correspond to narrow, medium, and wide width series, respectively. Independent of width, the multiple-ridge spacings stay the same and the corresponding wavenumbers assuming a wavelength equivalent to the ridge spacing are: $k_3 = 66\text{m}^{-1}$, $k_4 = 90\text{m}^{-1}$, $k_5 = 109$ m^{-1}, and $k_6 = 126\text{m}^{-1}$.

Table 1 Experimental parameters for each of the topography series dependent on single or multiple ridges present

Ridge Type	c (cm)	k_t (m^{-1})	k_n, k_m, k_w (m^{-1})	ϵ	Ex
Narrow: Single	2	59	44	0.88	0.07
Multiple	2	25	44	0.80–0.88	0.025
Medium: Single	3	42	31	0.58	0.043
Multiple	3	21	31	0.56–0.61	0.021
Wide: Single	4	33	24	0.47	0.033
Multiple	4	18	24	0.42–0.47	0.019

Additionally, criticality, ϵ, and excursion number, Ex, for each scenario are included in Table 1. Note that ϵ was always less than unity such that wave overturning and breaking was not expected near the topography (Balmforth et al. 2002). Ex was also much less than unity to prevent creation of local turbulence within the wavebeam (Jalali et al. 2014; Echeverri et al. 2009). The topography amplitudes are an order of magnitude smaller than the water depth to ensure wave radiation conditions are expected (Maas 2011; Papoutsellis et al. 2023). Another factor impacting the experimental results is Reynolds number, $Re = U_0^2/\omega\nu$, where ν is the kinematic viscosity of the liquid and U_0 is the topography velocity. For the experiments $Re \approx 10^2$, but for tidal flow in the ocean $Re \approx 10^7$. Thus, viscosity in the experiments is more important than in the ocean. Results may be altered (specifically the exact value of limits found) for the ocean, but general trends are expected to be similar.

Shadows of each ridge shape for the narrow topography are shown in Fig. 1 for visualization. Medium and wide topographies are similar shapes but with increasing width. The two control scenarios were the single-ridge and plateau scenarios. Results from these scenarios will represent the internal wave field expected from a single Gaussian of the same slope and shape as the ridges (Fig. 1a) as well as a flat top topography with no ridges but the same sloped sides and width as the multiple-ridge topographies (Fig. 1b). Since the flat top begins at the peak of each Gaussian ridge where the slope is zero, there is no discontinuity in slope and the transition from Gaussian to plateau is smooth. This topography also represents the case where the number of ridges goes to infinity.

To explore the impact of multiple ridges, three, four, five, and six ridges, respectively (Fig. 1c, e, g, & h), are included in the interior of the plateau. Each has the same overall length and maximum amplitude as the plateau and uses the same Gaussian shape for each ridge as the single-ridge

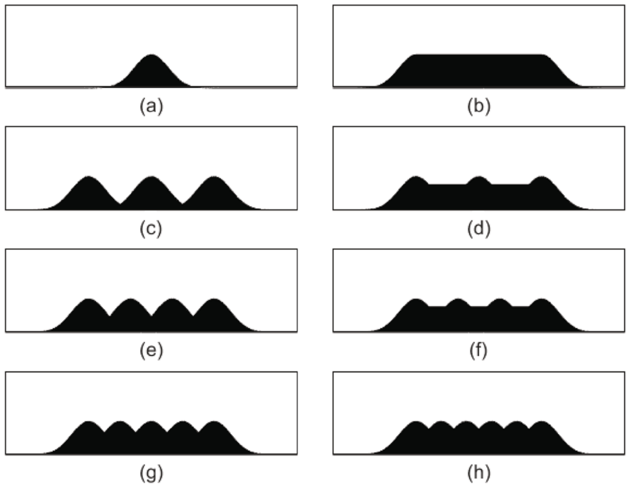

Fig. 1 Narrow topography shapes with Gaussian ridges (4 cm tall, single ridge width 8.6 cm, multiple ridge width 23.6 cm). Filled valleys have the same depth as the six-ridge topography valleys

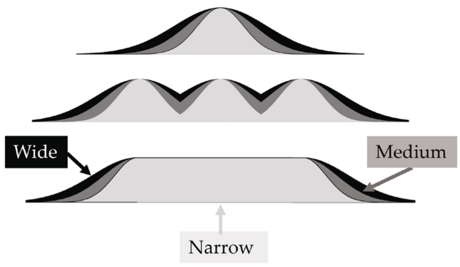

Fig. 2 Comparison of how increasing Gaussian width changes the topography lengths and overlap

topography. The end ridges are all at $b = \pm 7.5$ cm and have equally spaced central ridges, so that the spacing of the ridges decreases as the number of ridges increases. This results in shallower valleys between the ridges as the number of ridges increases. In order to examine how this influences the internal wave field, two more topographies corresponding to the three- and four-ridge cases are created with the valleys partially filled, as shown in Fig. 1(d) and (f). The depth of the fill is set to match that of the narrow six-ridge topography's valley depth. The transition between the ridges and the infill is smoothed using 5 mm fillets.

To investigate the impact of slope (decreasing ϵ) on internal wave generation, the above-described set of eight topographies was repeated for medium and wide Gaussian widths. A comparison of the topography widths is shown in Fig. 2. Since the outer ridges are located the same distance apart, the increasing Gaussian ridge width increases the amount of overlap between ridges and increases the overall topography length. For the multiple-ridge topographies, the increasing overlap results in decreased valley depth and thus decreased apparent amplitude of the interior ridge(s). In total, three widths (Fig. 2) of eight types of topographies (Fig. 1) for a total of 24 different topography shapes were examined. For each scenario, three tests were performed and kinetic energy results described in Sect. 2.2 were averaged over the tests.

3 Results and discussion

3.1 Qualitative results

An experiment for each case was run with the topography centered in the camera frame to visualize the internal waves generated from each side of the topography. Figure 3 shows the change in density gradient squared (ΔN^2) for all eight narrow topographies where the topography is located just above the images shown. Blue (negative) regions indicate a local decrease in squared stratification, and red (positive) regions indicate a local increase in squared stratification relative to the background stratification (N). Together these represent a single wavelength with both a vertical and horizontal component. Internal wave energy propagates away from the topography in the beams which emanate from the slopes of the topography then propagate downward to the left and right. The wave peaks and troughs move through the internal wave beam at the phase speed of the waves ($c_p \approx 0.01 m/s$): up and to the left for wave beams traveling down and left and up and to the right for wave beams traveling down and right. All narrow topographies were run at the same relative frequency ω/N of 0.81–0.83 such that the resulting internal waves form very similar angles to the vertical (θ) of about 36-38°. This is in line with Clark and Sutherland who reported that as topographic oscillation frequency increases relative to N, for ω/N values greater than 0.8, θ does not continue to decrease according to $\omega = Ncos(\theta)$ but stays below about 37° (Clark and Sutherland 2010).

For the single-ridge and plateau topographies shown in Fig. 3(a) and (h), approximately one wavelength is generated propagating each direction from each side of the topography. For the single ridge, the two beams are close enough to look like a single beam twice the width of the plateau beams. However, for all other topographies these waves bound the interior ridge generated internal waves (or lack thereof in the plateau case). For three- through six-ridge topographies shown in Fig. 3(b)-(g), waves are generated from each local slope such that in the near field a constructive/destructive interference pattern is observed immediately below the topography. The constructive interference between the left- and right-going beams forms local maxima and minima with larger amplitude (0.4–1.1 s^{-2} greater) than in either wave beam alone. These wave–wave interactions may contribute to the dispersion or dissipation of the interior (smaller) crests

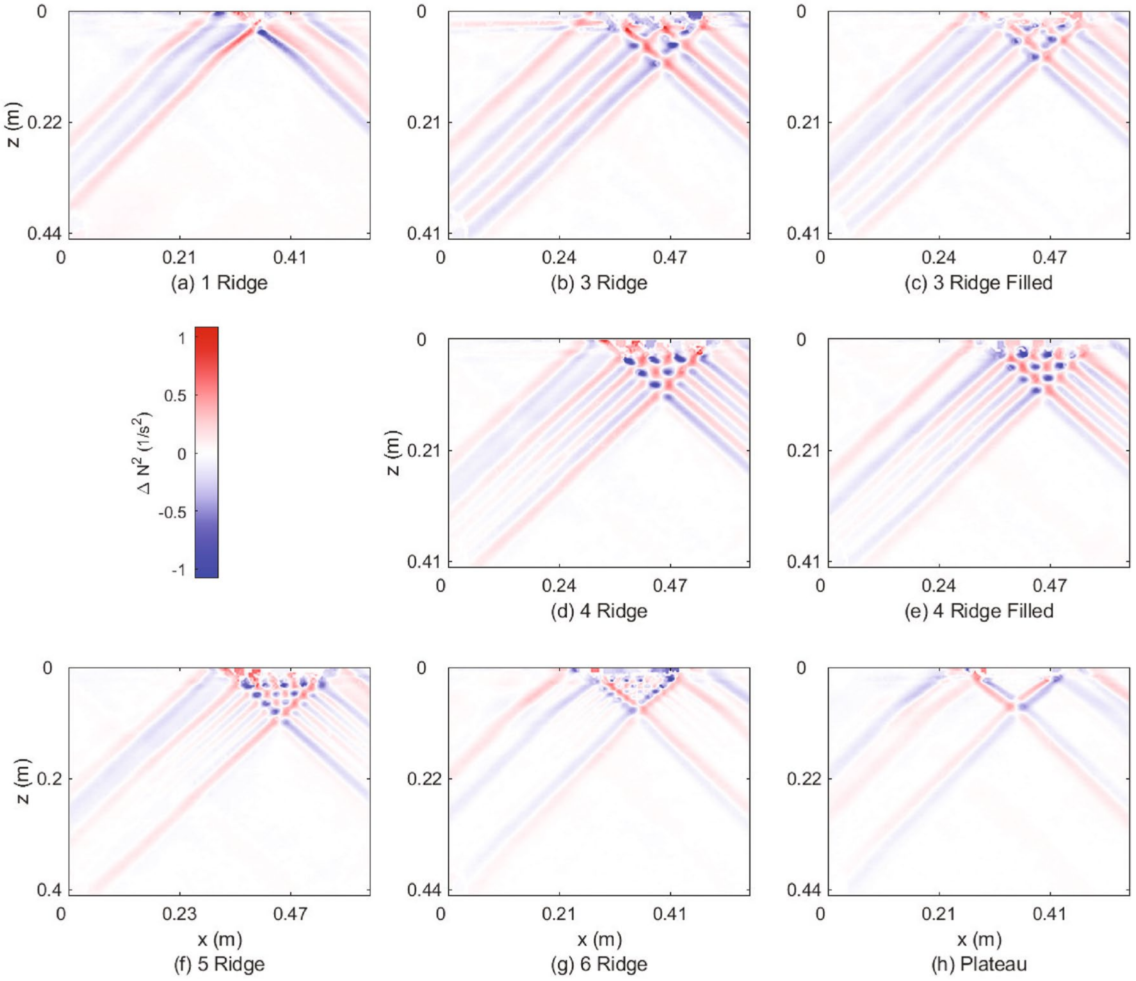

(a) 1 Ridge (b) 3 Ridge (c) 3 Ridge Filled

(d) 4 Ridge (e) 4 Ridge Filled

(f) 5 Ridge (g) 6 Ridge (h) Plateau

Fig. 3 Internal waves image with the ΔN^2 field for each of the narrow topographies. The topography is positioned above each image just to the right of center

between the two bounding waves in each beam observed for the four-, five-, and six-ridge topographies.

Both the filled version of the narrow three-ridge and four-ridge topographies are similar to the unfilled version (Fig. 3b-e). Each filled/unfilled pair generates the same number and wavelength of wave crests and troughs in each beam, but the three-ridge filled wave field has smaller amplitudes. This is expected because the three-ridge filled topography has a smaller apparent amplitude of the interior ridge due to the valleys on either side of that ridge being partially filled. The ΔN^2 amplitude is less disparate between the four-ridge and four-ridge filled topographies because the effective decrease in amplitude from partly filling in the valleys is smaller (there is already more ridge overlap, thus shallower valleys, in the four-ridge case) and higher wavenumbers associated with the shorter wavelengths result in less energy.

A gradual decay of internal wave amplitude during propagation becomes clear as the number of ridges increases, which is first seen for the four-ridge where there is a decrease of approximately 0.1 s^{-2} in ΔN^2 amplitude for the central wave beam crests and troughs relative to the bounding crests at the edges of the wave beam. This pattern of decay becomes even more visible in Fig. 3(f) for the five-ridge topography with the central crests nearly imperceptible by a depth of 0.2 m. Even starker is the wave field for the six-ridge topography where the central crests become indistinguishable shortly after the near-field interference region (Fig. 3(g)). This yields a wave field nominally the same as the plateau topography in the far-field region. Thus, the transition from multiple parallel crests within a wave beam to two separate crests is depicted from five to six ridges. One explanation for this occurrence is that since the total beam width (distance between the bounding crests) remains the same and more crests occur in the beam interior there are increased wave–wave interactions (or destructive interference and viscous dissipation) occurring just below the topography.

These interactions dissipate the internal waves faster than would occur without. A new non-dimensional number will be introduced which captures the impact of the topography scales on decreasing propagating energy. Further analysis of the propagating wave field parameters and a discussion of the reason for these dynamics will be included later in this section.

3.2 Quantitative results

Using Eq. 1 the *KE* of the downward, rightward propagating waves imaged is estimated, yielding Fig. 4. Small wavenumbers correspond to waves with large wavelengths and vice versa. Specifically, we define three characteristic horizontal wavenumbers (as defined in Sect. 2.3) based on (1) the overall topography width, k_t, (2) the single ridge width, k_n, k_m or k_w, and (3) the width of any interior ridges, $k_{spacing}$ where *spacing* ranges between 3 and 6 and is dependent on the number of interior ridges. The peak at the lowest value in each panel, $k = 21\text{m}^{-1}$, corresponds to a wavelength defined by the full beam width (or half in the case of the single ridge) which is characterized by the full topography width and excursion length. Note the spread in k for the single ridge is expected because the Gaussian profile is composed of more than one wavelength, which in turn generates waves with a range of wavelengths.

Three peaks are visible in each of the ridged and plateau topographies and are especially clear in the three-ridge topography, which correspond to k_t, k_n, and k_3. For the three-ridge filled topographies, the kinetic energy at the largest wavenumber decreases concomitant with the relative amplitude decrease from the three-ridge inner ridges. For each of the other topographies, as the ridge number increases, the contours become more similar to that of the plateau.

By summing the kinetic energy contours across the vertical wavenumber, m, kinetic energy as a function of the

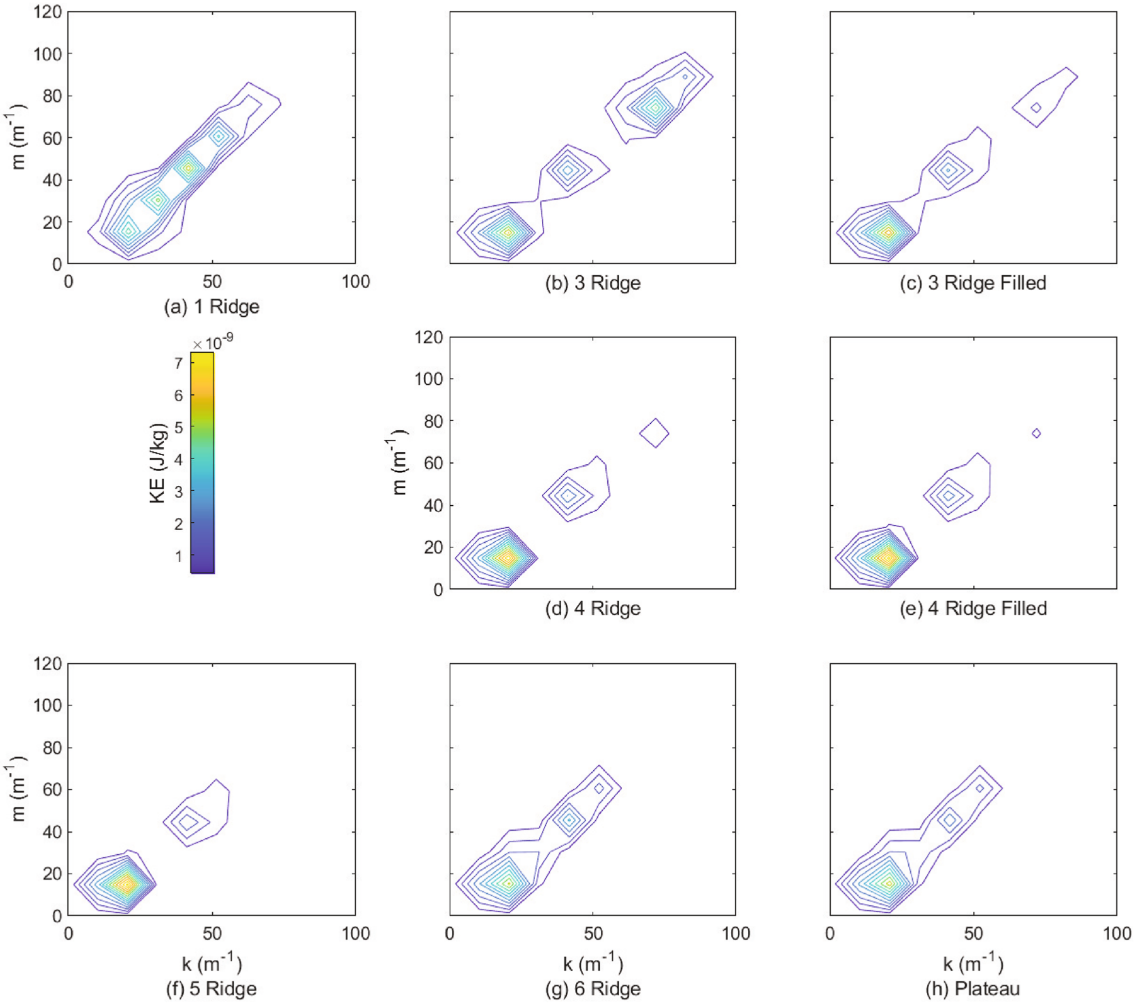

(a) 1 Ridge
(b) 3 Ridge
(c) 3 Ridge Filled
(d) 4 Ridge
(e) 4 Ridge Filled
(f) 5 Ridge
(g) 6 Ridge
(h) Plateau

Fig. 4 Kinetic energy values generated by each narrow topography across a range of wavenumbers. Note the x- and y-axis labels extend to upward and rightward panels, respectively

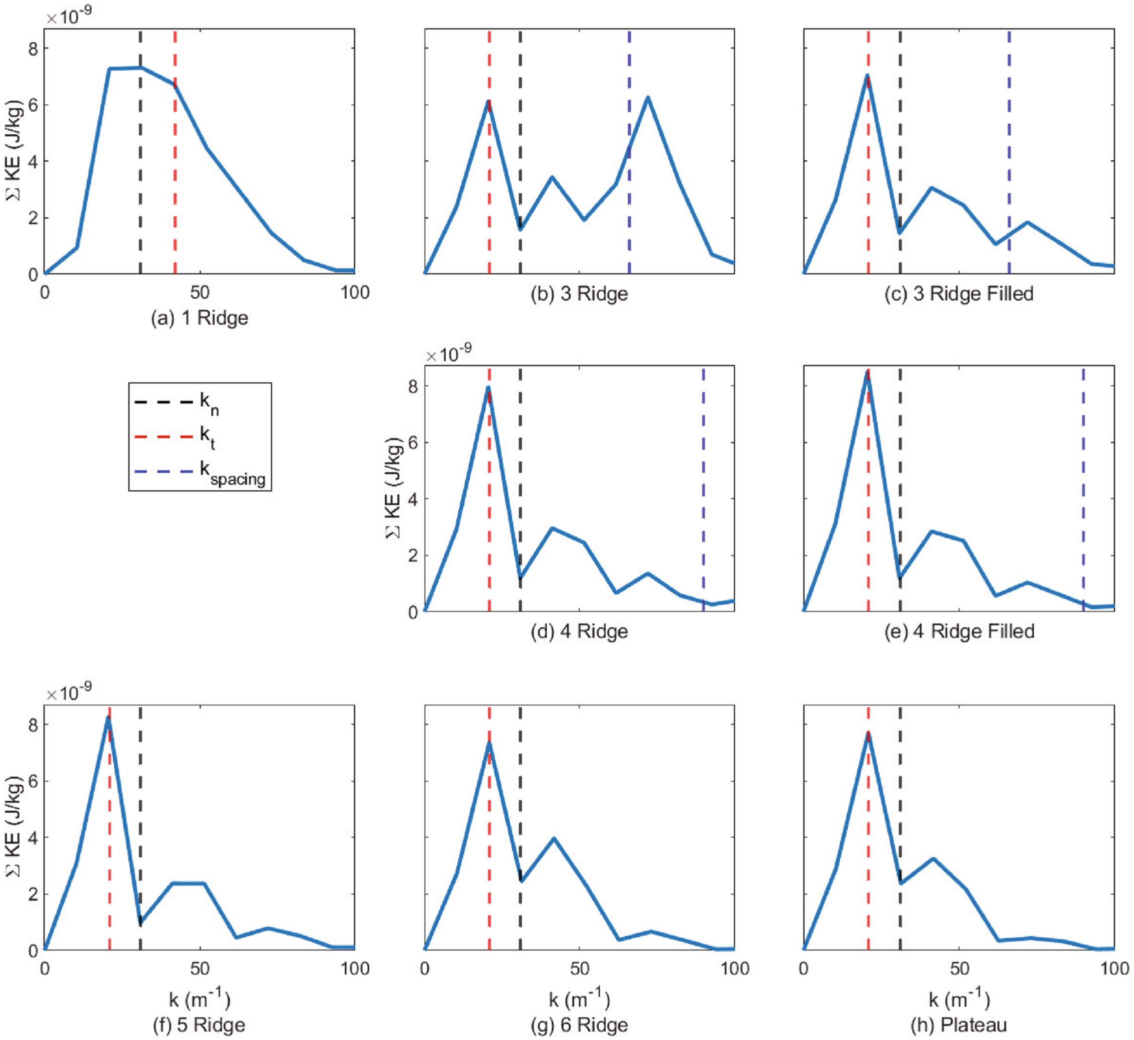

Fig. 5 Kinetic energy values generated by each narrow topography summed across *m*

horizontal wavenumber, *k*, is shown in Fig. 5. Vertical dashed lines are used to denote the expected *k* values based on the overall topography width (k_t), single ridge width (k_n), and the width of any interior ridges (k_3 to k_6). The distribution of kinetic energy with *k* for the narrow single-ridge topography is itself a single peak with a spread of values as can be seen in Fig. 5(a).

Here it is again clear that as the number of topography ridges increases from three to the plateau case, the kinetic energy decreases in higher wavenumbers and the kinetic energy profile approaches that of the plateau topography with more dominance of long wavelength motion. These topographies also have more kinetic energy at low wavenumbers compared to the single-ridge topography. This trend confirms that the topography width is dominant as the equivalent of ridge roughness becomes smaller. Additionally, the three peaks in *KE* are clear with the first one generally most prominent. Yet for the three-ridge topography, the third peak is significant and corresponds to the expected wavenumber defined by the width of the interior ridge, as mentioned previously.

Comparing the three-ridge with the three-ridge filled topography energy distribution (Fig. 5(b) and (c)), the lowest wavenumber energy peak is 15% higher for the filled topography, the mid wavenumber energy peak is 11% lower, and the high wavenumber energy peak is 71% lower on the filled topography. Interestingly, for the narrow series shown here the valley depth was decreased 70% by filling. Thus, filling in the topography valleys effectively decreases the ridge amplitude resulting in lower amplitude waves generated at high wavenumbers by the inner ridges and relatively more internal wave energy in the wavenumbers associated with the overall topography length.

Both the narrow four-ridge and four-ridge filled topographies' kinetic energy distributions are similar to that of the three-ridge filled distribution. The expected *k* wavenumber based on the overall topography width lines up with the main energy peak at the lowest wavenumbers. There is little kinetic energy at the expected *k* wavenumber for the interior ridge for either topography. The similarity in kinetic energy between the two four-ridge topographies may be due in part to the smaller filling needed for four peaks, which was only 55% of the original valley depth for the four-ridge as opposed to the 70% for the three-ridge.

All of the narrow five, six, and plateau topographies have significant kinetic energy peaks near the expected wavenumber based on the overall topography length. An intermediate wavenumber, secondary (magnitude) energy peak is also present for all of the long (three through plateau) topographies which is not clearly associated with an expected wavenumber. It occurs due to the distribution of wavenumbers generated by a single Gaussian ridge as can be observed by the single-ridge topography's kinetic energy spread including those wavenumbers. The third *KE* peak at higher wavenumber is much smaller, an order of magnitude smaller in the plateau case. These general trends are seen for all width series.

To normalize the data, the kinetic energy is summed across both the horizontal (k) and vertical (m) wavenumbers and a total kinetic energy generation is estimated for each topography. These values are listed in Table 2. This is necessary as the different shapes and sizes generate different total kinetic energies and some variability is introduced by the camera position relative to the topography (1-4 cm below). The summed kinetic energy of Fig. 5 normalized by the total *KE* tabulated in Table 2 results in $\sum \widehat{KE}$ and is shown in Fig. 6.

All of the four- through six-ridge topographies have $\widehat{KE}$ distributions that are similar to the plateau which has a dominant low wavenumber peak and a secondary higher wavenumber peak. By normalizing the kinetic energy, the main energy peak for these topographies is shown to contribute the following percentage of the total kinetic energy generated for the respective topography: 35% (four-ridge), 42% (five-ridge), 36% (six-ridge), and 39% (plateau). They also have approximately the same percentage of kinetic energy at $k \approx 10$, ≈ 50, ≈ 60 $\mathrm{m^{-1}}$, and above $k \approx 80$ $\mathrm{m^{-1}}$. The four- and five-ridge narrow topographies diverge slightly at $k \approx 30$ and ≈ 41 $\mathrm{m^{-1}}$ where they are $5-6\%$ lower than the plateau. Of the multi-ridge topographies, the three-ridge topography profile differs the most from the plateau topography, especially between $k \approx 51$ and ≈ 92 $\mathrm{m^{-1}}$. As was discussed previously, the narrow three-ridge profile represents only slightly overlapping ridges such that each individual ridge contributes to the generated internal wave field. In addition, when directly comparing the four- and five-ridge, $\widehat{KE}$ shows that the four-ridge topography has a slightly higher percentage in higher wavenumbers associated with interior ridges than the five-ridge, which is why the five-ridge topography has a higher percentage at $k \approx 20$ $\mathrm{m^{-1}}$.

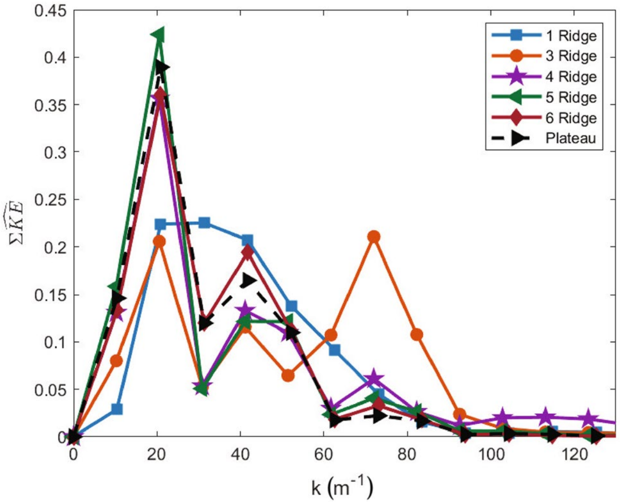

Fig. 6 Normalized kinetic energy ($\widehat{KE}$) values generated by the single-ridge, three-ridge, four-ridge, five-ridge, six-ridge, and plateau narrow width topographies summed across m. The plateau line is dashed to help visualize the lines that have similar kinetic energy. Each line is normalized by the total kinetic energy generated by the respective topography

Table 2 Total kinetic energy for the narrow, medium, and wide topographies

	Total kinetic energy ($\times 10^{-9}$) (J/kg)		
Number of ridges	Narrow	Medium	Wide
1	32.4	23.7	23.6
3	29.7	20.4	13.7
3 Filled	21.7	16.7	14.1
4	22.3	17.8	13.5
4 Filled	21.7	17.1	12.9
5	19.5	13.6	11.9
6	20.4	15.2	11.9
Plateau	19.8	16.0	11.5

As the number of ridges increases for the same overall topography length, the generated internal wave field approaches that of the plateau topography. Thus, the impact of individual ridges is increasingly negligible as the number of ridges increases. This is important to note for realistic topographies with many small random ridges and roughness. Partly filling in the valleys for the three- and four-ridge topographies results in decreased kinetic energy at higher wavenumbers associated with the inner ridges. This stems from the decrease in apparent amplitude of the interior topography ridges.

Next we explore the summed, normalized *KE* for the medium-width topographies, shown in Fig. 7. Similar to

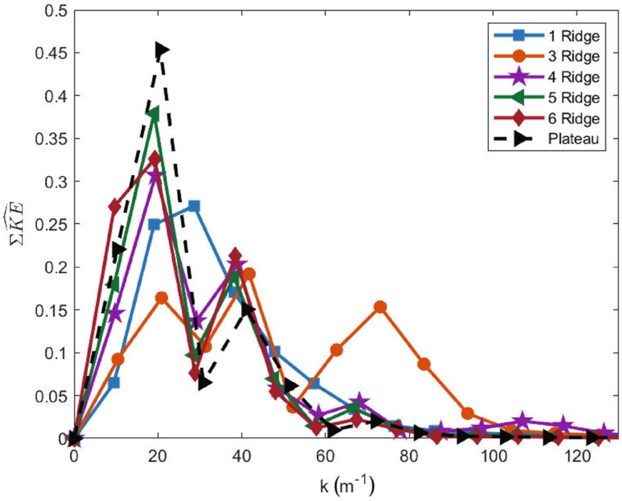

Fig. 7 Normalized kinetic energy ($\widehat{KE}$) values generated by the single-ridge, three-ridge, four-ridge, five-ridge, six-ridge, and plateau medium width topographies summed across m. The plateau line is dashed to help visualize the lines that have similar kinetic energy. Each line is normalized by the total kinetic energy generated by the respective topography

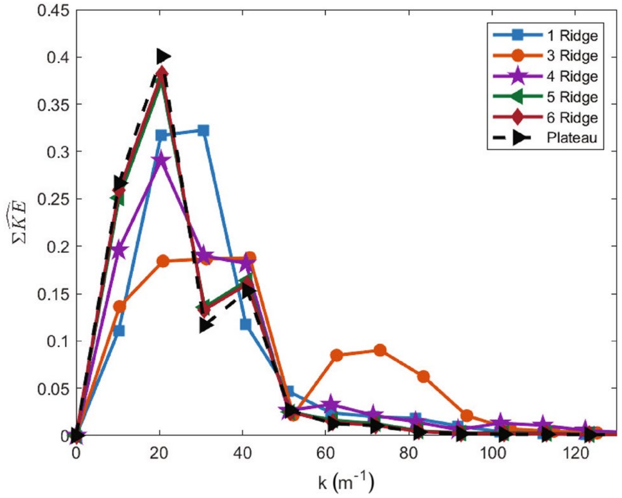

Fig. 8 Normalized kinetic energy ($\widehat{KE}$) values generated by the single-ridge, three-ridge, four-ridge, five-ridge, six-ridge, and plateau wide width topographies summed across m. The plateau line is dashed to help visualize the lines that have similar kinetic energy. Each line is normalized by the total kinetic energy generated by the respective topography

the narrow topographies, $\widehat{KE}$ peaks correlate to expected wavenumbers (which are lower for all of the medium topographies because the Gaussian is wider) and a greater spread is observed for the single-ridge topography. All of the long (three through plateau) topographies have $\widehat{KE}$ associated with the overall topography length ($k \approx 20$ m^{-1}) and single ridge width $k \approx 40$ m^{-1}. Note here the energy is concentrated at $k = 40\text{m}^{-1}$ where the narrow topographies had a broader peak extending to $k = 50\text{m}^{-1}$. The main energy peak for these topographies is shown to contribute the following percentage of the total kinetic energy generated for the respective topography: 31% (four-ridge), 38% (five-ridge), 33% (six-ridge), and 45% (plateau).

Three-ridge through plateau-medium topographies have similar amplitude $\widehat{KE}$ peaks near the expected wavenumber based on the interior ridges, though the plateau has the lowest. The three-ridge also has a comparable amplitude peak in $\widehat{KE}$ based on the single ridge width which shows the importance of each of the ridge widths (overall, single, and interior) for wave generation by this topography. Generally, the $\widehat{KE}$ profile approaches that of the medium plateau as the number of ridges increases.

Finally, for the wide series, normalized summed kinetic energy profiles are shown in Fig. 8. These results are similar to the narrow and medium series, with lower energy at large wavenumbers, a single peak for energy generated by the single-ridge topography, and energy peaks that align with expected wavenumber peaks. Notable differences include a further shift to lower wavenumbers due to the wider Gaussian and a lower peak near $k = 41$ m^{-1} associated with the single-ridge wavelength which means the wave generation is dominated by the overall topography width.

Additionally the three-ridge topography does not generate three kinetic energy peaks (like in the narrow and medium series); rather, it generates two wide kinetic energy peaks. The energy peak at smaller k values covers wavenumbers associated with both the single ridge and overall topography length, while the peak at larger k values occurs at the wavenumber associated with the interior ridge width. This indicates that the interior ridge, k_3, does still contribute to the kinetic energy (24%) in the internal waves, but the longer wavelengths of the single ridge and overall topography length contribute more (70%) where their individual contributions cannot be accurately estimated.

Across all wavenumbers the five-ridge, six-ridge, and plateau topographies are nearly indistinguishable ($\widehat{KE}$ differs by less than 2.6% anywhere). Above $k \approx 50$ m^{-1}, the four-ridge topography also has very similar $\widehat{KE}$ as the plateau, but at lower wavenumbers the four-ridge energy distribution has a broader peak resulting in lower $\widehat{KE}$ at each individual wavenumber.

Especially for the wide topographies, where the wider inner ridges have greater overlap, as the number of ridges increases, the overall shape of the topography looks more like a plateau with small-scale roughness. It is therefore unsurprising that a smaller percentage of the kinetic energy is generated at higher wavenumbers as the number of topography ridges increases.

3.3 Ridge width comparison

To account for kinetic energy in low, mid, and high wavenumber ranges, three k bins were created (k = 0-42, 42-94, 94-146 m^{-1}). The summed kinetic energy was calculated for each bin and plotted in Fig. 9. The three k ranges were chosen so that the first two peaks, which represent the topography width and shape, are combined in the first bin; the second bin captures the interior wavenumber associated with the three-ridge, k_3; and the third bin is the highest wavenumbers observed. Five data points from Figs. 6 to 8 fall into each bin for each topography, generally. These normalized values are multiplied by the total kinetic energy in each scenario to present a dimensional KE. Due to the slight variations in camera distance across tests and the pixel-to-meter calibration, the slight variance in k spacing is just enough that six medium topographies (single-, three filled, four-, four filled, five-, and six-ridge) have six data points in the k =94-146 m^{-1} range and thus these bins were averaged and multiplied by 5/6 to get the approximate equivalent of five points.

Every topography in every series (narrow, medium, and wide) exhibits decreasing kinetic energy with increasing k bin, except the narrow three-ridge topography. This is expected because longer wavelengths (smaller wavenumbers) carry more kinetic energy than do shorter wavelengths, so large wavenumbers have less kinetic energy overall. In the case of the narrow three-ridge topography, the total kinetic energy in the second bin is $KE = 1.53\times10^{-8}$ J/kg, which is slightly greater than in the first bin where $KE = 1.35\times10^{-8}$ J/kg due to the large energy peak described previously in Fig. 5(b).

Total kinetic energy also decreases with increasing topography width for all of the bin categories as expected based on the results of prior studies (Laurent et al. 2003;

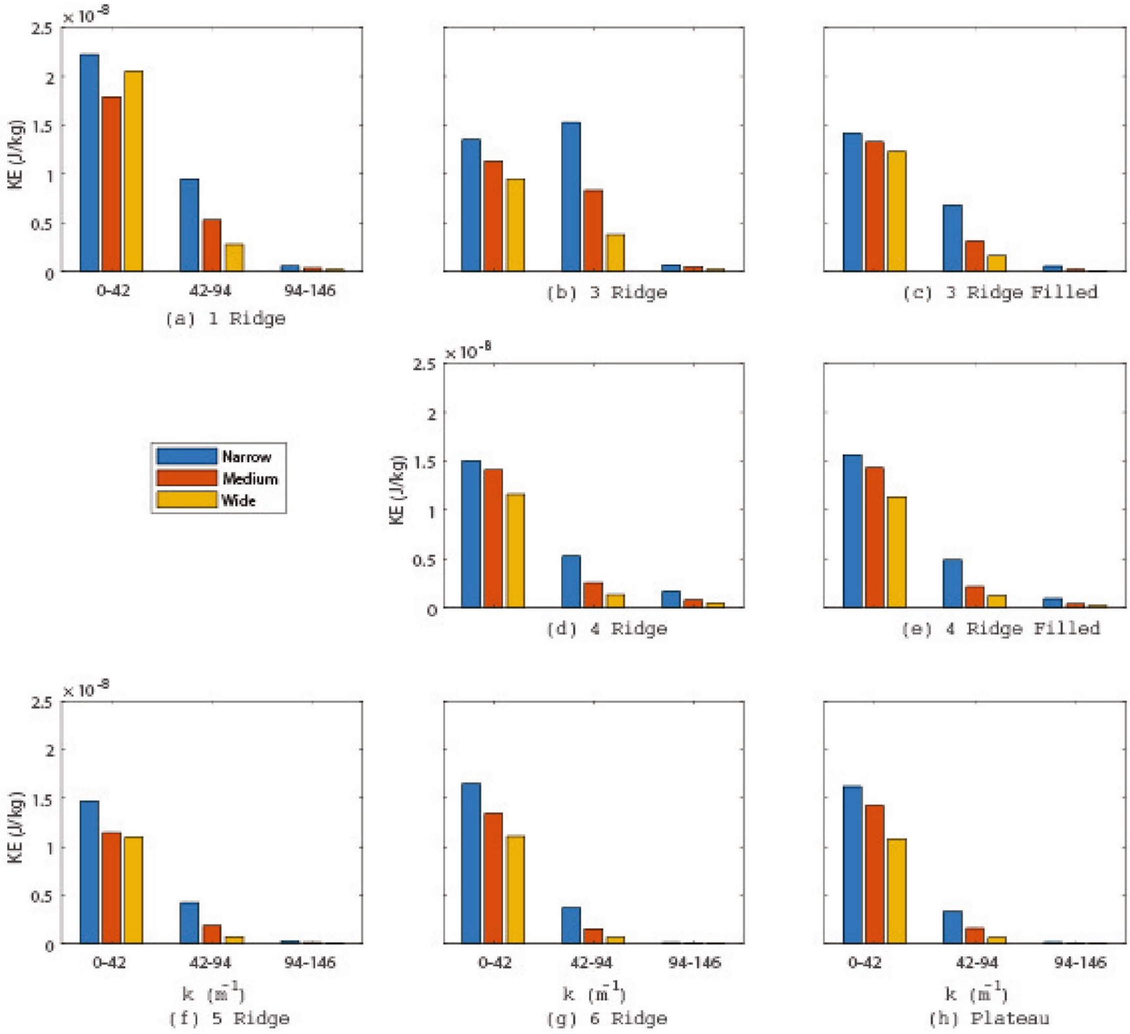

Fig. 9 Kinetic energy summed into three bins based on k ranges for each topography in the narrow, medium, and wide series

Hakes and Crockett 2024). Additionally, due to the same spacing for multiple ridges, the medium and wider series have shallower valleys than the narrow. Specifically, the medium valleys are 34% shallower than the narrow and the wide are 57% more shallow. Thus, the energy in the second set of bins decreasing with width is consistent with the amplitude of the generating peaks and is consistent throughout the ridges. The only exception to this is for the medium and wide single-ridge topographies in the first bin range. This occurs because the wide single-ridge topography generates kinetic energy at a smaller range of wavenumbers (Fig. 8) as was mentioned previously.

Comparing the ridged topographies directly to the plateau provides insight into when the wave field generated is indistinguishable from that generated by the plateau. The filled shapes are not included and only the first two bins are compared since they contain over 97% of the *KE* (except in the narrow four-ridge case where it is 92%). To compare, the plateau $\widehat{KE}$ in each bin is subtracted from the ridge $\widehat{KE}$ in each bin and divided by the average *KE* between them to estimate the percent difference. However, since each bin has a different contribution to the total, this is then multiplied by the average percent of *KE* in the bin, thus resulting in just the difference in $\widehat{KE}$ in each bin from the plateau. It represents the difference in percentage of *KE* in each bin between the ridge number shown and the plateau and demonstrates how similar each portion of the generated wave field is to the plateau. Results are shown in Fig. 10. For each scenario the lowest wavenumber bin in the ridged case is less than that of the plateau and is therefore negative. The next bin is always positive as the higher wavenumber waves in the ridge cases are more energetic. These bars clearly show that as topography width or number of ridges increases, the difference from the plateau drops significantly.

To capture this trend toward plateau-like wave generation more directly, we introduce a ratio of lengths. Specifically, the total length of the expected wavebeam ($L_t = L + p$) to the total length needed to fit all the expected wavelengths (L_w =(Number of ridges + 1)$*$ $(w + p)$). Values of L_t/L_w are shown in Table 3. When this non-dimensional number is less than ≈ 0.3, physically less than 1/3 of a wavelengths fit in the beam and there is destructive interference and viscous dissipation as the waves interact. Although waves of the expected wavelength are generated in the near field, as is seen in Fig. 3, they decay almost immediately. Thus, $L_t/L_w \leq 0.3$ represents a limit for when waves generated by the local ridge shape will decay immediately in the near field such that the far field will be identical to that of the plateau. Above this there is not necessarily a clear dependence on *KE* increasing or decreasing as the L_t/L_w number continues to increase and the local resonance may impact the results. When compared with Fig. 10, these values correspond to scenarios where the total difference between the ridges and plateau (sum of each bin) is less than 15%. In addition, when the non-dimensional ratio of expected wavenumbers squared is small, for example $(k_t/k_3)^2 < 0.1$, kinetic energy will likely be negligible at the interior ridge wavenumber due to its relatively high wavenumber (note in the *KE* calculation ΔN^2 is multiplied by k^{-2}). Although this is not a deciding factor here, we note it since in other scenarios it

Table 3 Suggested non-dimensional number, L_t/L_w, providing cutoff estimate for the impact of ridges. In parenthesis is $(k_t/k_{spacing})^2$. The number of ridges is shown at the top of each column, and the series size is shown for each row. Filled are the same as their unfilled counterpart and are not shown. Plateau-type wave generation is expected for highlighted cells

	Number of Ridges			
Width	3	4	5	6
Narrow	0.45 (0.10)	0.36 (0.05)	**0.30 (0.03)**	**0.26 (0.02)**
Medium	0.37 (0.07)	**0.30 (0.03)**	**0.25 (0.02)**	**0.21 (0.01)**
Wide	0.32 (0.06)	**0.26 (0.02)**	**0.22 (0.01)**	**0.19 (0.01)**

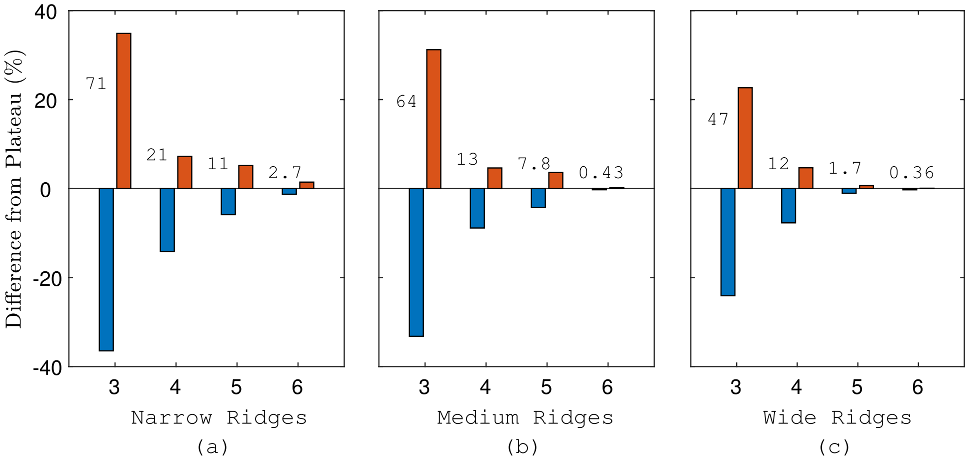

Fig. 10 Difference in normalized kinetic energy between ridged topographies and the plateau contained in each of the two first wavenumber bins (blue is $k = 0 - 42\text{m}^{-1}$ and red is $k = 42 - 94\text{m}^{-1}$). Narrow results are in (a), medium in (b), and wide in (c). Included above each set of bars is a value representing the total percentage difference from the plateau when the absolute values of the two bin difference values are summed

may be important. Thus, we have found for scenarios where $L_t/L_w \leq 0.3$ and $(k_t/k_3)^2 < 0.1$ the propagating internal wave field generated by the topography will be independent of ridge presence.

4 Conclusions

An experimental exploration of the impact of topography ridges in stratified oscillating flows was accomplished. The internal wave field generated by these topographies was compared with that generated by a smooth plateau topography. Results show that as the topography width increases the ridges have a smaller impact on the overall generated wave field. Additionally, as the number of ridges increases for a given width, the waves generated by the ridges begin to destructively interfere and further dissipation occurs. Once four to six ridges are present (for these scenarios), their impact on the far-field wave field is negligible when compared with the plateau. In the near-field, internal waves generated by ridges are clearly observed in the wavebeam but decay quickly as they propagate. However, the number of ridges alone is not the direct deciding factor for internal wave propagation. A non-dimensional number is suggested which captures the dynamics observed from both the topography width and the number of ridges which represents the width of the wavebeam relative to the width necessary for the waves generated by each ridge to be fully contained in the wavebeam. When $L_t/L_w \leq 0.3$, the wavebeam is not wide enough for all of the generated waves to propagate and the far-field wave field may be approximated by an internal wave field generated by the plateau. Thus, for these scenarios the impact of ridges, or topography roughness, is expected to be negligible. Evaluating how these results would scale to the ocean, the decreased relative impact of viscosity (much larger *Re*) may delay the transition to a plateau-like wave field to smaller L_t/L_w as the viscous dissipation of the smaller scale waves would be mitigated.

Author contributions Authors contributed equally.

Funding This work has been supported by the Utah NASA Space Grant Consortium and by NSF Grants CBET-1606040 and OCE-2343089.

Data availability statement Data are available through contacting the corresponding author.

Code availability Not applicable.

Declarations

Conflict of interest The authors have no conflict of interest to disclose.

Ethics approval and consent to participate Not applicable.

Consent for publication Authors consent to publication of this manuscript.

Materials availability Not applicable.

References

Aguilar DA, Sutherland BR (2006) Internal wave generation from rough topography. Phys Fluids 18. https://doi.org/10.1063/1.2214538

Balmforth NJ, Ierley GR, Young WR (2002) Tidal conversion by subcritical topography. J Phys Oceanogr 32(10):2900–2914. https://doi.org/10.1175/1520-0485(2002)032<2900:TCBST>2.0.CO;2

Balmforth NJ, Peacock T (2009) Tidal conversion by supercritical topography. J Phys Oceanogr 39(8):1965–1974. https://doi.org/10.1175/2009JPO4057.1

Clark HA, Sutherland BR (2010) Generation, propagation, and breaking of an internal wave beam. Phys Fluids 22:1–16 https://doi.org/10.1063/1.3455432

Dalziel SB, Hughes GO, Sutherland BR (2000) Whole-field density measurements by 'synthetic schlieren'. Exp Fluids 28:322–335

Dalziel Research Partners: DigiFlow (2018)

Echeverri P, Yokossi T, Balmforth NJ, Peacock T (2011) Tidally generated internal-wave attractors between double ridges. J Fluid Mech 669:354–374

Echeverri P, Peacock T (2010) Internal tide generation by arbitrary two-dimensional topography. J Fluid Mech 659:247–266. https://doi.org/10.1017/S002211201000241

Echeverri P, Flynn MR, Winters KB, Peacock T (2009) Low-mode internal tide generation by topography: an experimental and numerical investigation. J Fluid Mech 636:91–108. https://doi.org/10.1017/S0022112009007654

Egbert GD, Ray RD (2000) Significant dissipation of tidal energy in the deep ocean inferred from satellite altimeter data. Nature 405:775–778. https://doi.org/10.1038/35015531

Garett C, Kunze E (2007) Internal tide generation in the deep ocean. Ann Rev Fluid Mech 39:57–87. https://doi.org/10.1146/annurev.fluid.39.050905.110227

Hakes K, Crockett J (2024) Internal waves generated from asymmetric topographies. Exp Thermal Fluid Sci 157:111240. https://doi.org/10.1016/j.expthermflusci.2024.111240

Jalali M, Rapaka NR, Sarkar S (2014) Tidal flow over topography: Effect of excursion number on wave energetics and turbulence. J Fluid Mech 750:259–283. https://doi.org/10.1017/jfm.2014.258

Klymak JM, Balwada D, Garabato AN, Abernathey R (2021) Parameterizing nonpropagating form drag over rough bathymetry. J Phys Oceanogr 51(5):1489–1501. https://doi.org/10.1175/JPO-D-20-0112.1

Lamb KG (2014) Internal wave breaking and dissipation mechanisms on the continental slope/shelf. Ann Rev Fluid Mech 46(Volume 46, 2014), 231–254. https://doi.org/10.1146/annurev-fluid-011212-140701

Laurent LS, Stringer S, Garrett C, Perrault-Joncas D (2003) The generation of internal tides at abrupt topography. Deep-Sea Res Part I: Oceanogr Res Papers 50:987–1003. https://doi.org/10.1016/S0967-0637(03)00096-7

Lee A, Crockett J (2019) Turning depths: Evanescent to propagating wave kinetic energy density. Phys Rev Fluids 4(3):34803. https://doi.org/10.1103/PhysRevFluids.4.034803

Maas LRM (2011) Topographies lacking tidal conversion. J Fluid Mech 684:5–24. https://doi.org/10.1017/jfm.2011.245

Munk W, Wunsch C (1989) Abyssal recipes ii: energetics of tidal and wind mixing. Deep-Sea Res Part I 45:239–270. https://doi.org/10.1016/b978-0-12-751800-8.50016-1

Nycander J (2006) Tidal generation of internal waves from a periodic array of steep ridges. J Fluid Mech 567:415–432. https://doi.org/10.1017/S002211200600228X

Nappo CJ (2002) An Introduction to Atmospheric Gravity Waves. Academic Press, San Diego, California

Nelson AD, Arbic BK, Menemenlis D, Peltier WR, Alford MH, Grisouard N, Klymak JM (2020) Improved internal wave spectral continuum in a regional ocean model. J Geophys Res: Oceans 125(5):2019–015974. https://doi.org/10.1029/2019JC015974 https://agupubs.onlinelibrary.wiley.com/doi/pdf/10.1029/2019JC015974. e2019JC015974 10.1029/2019JC015974

Papoutsellis CE, Mercier MJ, Grisouard N (2023) Internal tide generation from non-uniform barotropic body forcing. J Fluid Mech 964:20. https://doi.org/10.1017/jfm.2023.358

Scott RB, Goff JA, Naveira Garabato AC, Nurser AJG (2011) Global rate and spectral characteristics of internal gravity wave generation by geostrophic flow over topography. J Geophys Res: Oceans https://doi.org/10.1029/2011JC007005

Sutherland BR, Aguilar DA (2006) Stratified flow over topography: Wave generation and boundary layer separation. WIT Trans Eng Sci 52:317–326. https://doi.org/10.2495/AFM06032

Sutherland BR, Dalziel SB, Hughes GO, Linden PF (1999) Visualization and measurement of internal waves by 'synthetic schlieren'. part 1. vertically oscillating cylinder. J Fluid Mech 390:93–126. https://doi.org/10.1017/S0022112099005017

Trossman DS, Arbic BK, Garner ST, Goff JA, Jayne SR, Metzger EJ, Wallcraft AJ (2013) Impact of parameterized lee wave drag on the energy budget of an eddying global ocean model. Ocean Model 72:119–142. https://doi.org/10.1016/j.ocemod.2013.08.006

Wunsch S, Brandt A (2012) Laboratory experiments on internal wave interactions with a pycnocline. Exp Fluids 53:1663–1679. https://doi.org/10.1007/s00348-012-1387-0

Wunsch C (1998) The work done by the wind on the oceanic general circulation. J Phys Oceanogr 28:2332–2342. https://doi.org/10.1175/1520-0485(1998)028<2332:twdbtw>2.0.co;2

Zhang L, Swinney HL (2014) Virtual seafloor reduces internal wave generation by tidal flow. Phys Rev Lett 112:104502. https://doi.org/10.1103/PhysRevLett.112.104502

Zhang L, Buijsman MC, Comino E, Swinney HL (2017) Internal wave generation by tidal flow over periodically and randomly distributed seamounts. J Geophys Res: Oceans 122(6):5063–5074. https://doi.org/10.1002/2017JC012884 https://agupubs.onlinelibrary.wiley.com/doi/pdf/10.1002/2017JC012884